

JGR Solid Earth

RESEARCH ARTICLE

10.1029/2020JB021222

Key Points:

- Greigite was identified as the major magnetic mineral in almost 4-m-thick late MIS 3 sediments from the outer shelf of the East China Sea
- Authigenic greigite and pyrite have great potential to indicate sea-level change on continental shelves even on suborbital timescales
- Water depths of 30–60 m are likely to be more suitable for extensive formation and preservation of greigite in continental shelf sediments

Supporting Information:

- Supporting Information S1
- Table S1

Correspondence to:

J. Liu and X. Shi,
ljsx880116@163.com;
xfshi@fio.org.cn

Citation:

Liu, J., Shi, X., Liu, Q., Liu, S., Liu, Y., Zhang, Q., et al. (2021). Authigenic iron sulfides indicate sea-level change on the continental shelf: An illustration from the East China Sea. *Journal of Geophysical Research: Solid Earth*, 126, e2020JB021222. <https://doi.org/10.1029/2020JB021222>

Received 19 OCT 2020
 Accepted 7 FEB 2021

© 2021. American Geophysical Union.
 All Rights Reserved.

Authigenic Iron Sulfides Indicate Sea-Level Change on the Continental Shelf: An Illustration From the East China Sea

Jianxing Liu^{1,2} , Xuefa Shi^{1,2} , Qingsong Liu^{2,3}, Shengfa Liu^{1,2} , Yan Liu⁴, Qiang Zhang⁵ , Xiaoxiao Yu⁶ , Xisheng Fang^{1,2} , Yonghua Wu^{1,2}, Taoyu Xu^{1,2}, and Jinhua Li^{2,4} 

¹Key Laboratory of Marine Geology and Metallogeny, First Institute of Oceanography, Ministry of Natural Resources (MNR), Qingdao, China, ²Laboratory for Marine Geology, Pilot National Laboratory for Marine Science and Technology, Qingdao, China, ³Centre for Marine Magnetism (CM2), Department of Ocean Science and Engineering, Southern University of Science and Technology, Shenzhen, China, ⁴Key Laboratory of Earth and Planetary Physics, Institute of Geology and Geophysics, Chinese Academy of Sciences, Beijing, China, ⁵State Key Laboratory of Lithospheric Evolution, Institute of Geology and Geophysics, Chinese Academy of Sciences, Beijing, China, ⁶State Key Laboratory of Isotope Geochemistry, Guangzhou Institute of Geochemistry, Chinese Academy of Sciences, Guangzhou, China

Abstract Although sea-level is the primary control over sedimentary architectures on continental shelves, deciphering such changes is still challenging, except for the easily recognized transgression-regression cycles. This problem becomes more prominent in sedimentary units with relatively homogenous and fine-grained lithologies that have been deposited over short periods. Here, we focus on a dominantly clayey silt section of a sediment core from the outer shelf of the East China Sea. Detailed rock magnetic and electron microscopy analyses indicate that authigenic greigite (Fe₃S₄) is the major magnetic component in an almost 4-m-thick interval that was deposited during the late Marine Isotope Stage (MIS) 3, while pyrite (FeS₂) is enriched in the underlying middle MIS 3 sediments. According to microfossil analyses, the identified greigite formed in a prodelta setting that was affected by cold coastal currents after the middle MIS 3, when the Taiwan Warm Current and its associated upwelling were prevailing within a middle-outer shelf setting favorable for pyrite formation. Large-amplitude regression occurred subsequently during the MIS 2, limiting sulfate supply and favoring the greigite preservation. Our results, along with the previous studies, demonstrate that both the material and environmental conditions that are crucial to iron sulfide survival have been largely controlled by sea-level change. Moreover, we make a preliminary proposition that a water depth range of 30–60 m is more likely to lead to the enrichment of greigite on continental shelves. We, therefore, provide a promising avenue for the assessment of sea-level change on continental shelves over orbital and even suborbital timescales.

1. Introduction

Driven by glacio-eustatic processes, the Earth has experienced a phase of large-amplitude sea-level change as intensive as any during its history since the Quaternary (Rohling et al., 2014), which has branded profound imprints in marine sediments. For example, with regard to deep-sea sediments, a remarkable feature is the variations in the oxygen isotope records of benthic foraminifera (BF), such as the well-known “LR04 stack” (Lisiecki & Raymo, 2005). Likewise, for sedimentary records on continental shelves, which serve as a link between the land and the deep ocean, sea-level fluctuations over glacial-interglacial timescales (e.g., the cycles in the Earth’s orbital eccentricity of ~100-kyr) are generally expressed as transgression-regression cycles (Shi et al., 2016). Due to their wide and gentle landforms, as well as relatively shallow water depths, continental shelves are much more sensitive to sea-level changes than abyssal regions; even trifling fluctuations in sea-level can give rise to considerable shoreline migration (Yao et al., 2020). Nevertheless, besides the easily identified transgression-regression cycles, it is difficult to trace changes in sea-level over much shorter timescales, which, however, is of great significance to human activities in coastal areas (Yang et al., 2015). This problem is more prominent in relation to sedimentary units with homogenous lithologies, especially for fine-grained sediments which are relatively poor in BF due to high sedimentation rates and

hypoxia (Osterman, 2003). In addition, the oxygen isotope values of BF within such areas are sometimes more affected by local salinity rather than temperature (Xu & Oda, 1999).

The formation, transportation, deposition, and postdepositional alterations of magnetic minerals are sensitive to a wide range of environmental processes, which emphasizes the usefulness of magnetic measurements in environmental studies (Liu et al., 2012). Specifically, primary (i.e., depositional) magnetic minerals, mainly iron oxides, provide information about sediment source areas and transportation pathways, while secondary magnetic minerals such as authigenic iron sulfides indicate diagenetic changes depending on the redox conditions in depositional environments (Fu et al., 2008). Among the various iron sulfides, greigite (Fe_3S_4) is remarkable in that it shares a similar magnetic lattice to magnetite and thus is strongly ferrimagnetic (Skinner et al., 1964). As a precursor to paramagnetic pyrite (FeS_2), which is ubiquitous in sulfidic marine sediments, greigite has often been ignored due to its lower stability relative to pyrite and poor detectability by geochemical and mineralogical analytical methods (Roberts & Weaver, 2005). Nevertheless, the development of modern superconducting rock magnetometers during the last 40 years has resulted in an increasing number of reports about sedimentary greigite, largely due to its paleomagnetic importance (Roberts et al., 2011), with magnetic studies of synthetic greigite expanding our the knowledge of this “young” magnetic mineral (Chang et al., 2007, 2008). Moreover, the formation and preservation of greigite require relatively high Eh conditions, making its environmental implications more distinctive (Kao et al., 2004).

In recent years, greigite has been identified widely in continental shelf sediments (e.g., Mohamed et al., 2011; Nilsson et al., 2013; Oda & Torri, 2004), especially in the shelf seas that lie extensively off the eastern coast of China and which connect the largest continent (i.e., Eurasia) with the ocean (i.e., the Pacific), which has provided deep insights into the formation and preservation mechanisms of greigite (e.g., Ge et al., 2015; Liu et al., 2004, 2018; Zheng et al., 2010). Interestingly, these studies imply that the identified greigite and its end-product, that is, pyrite, both have relations with sea-level change, which inspires further investigations to uncover the underlying key mechanisms. We, therefore, attempt in this work to clarify this issue via an integrative study of rock magnetism, mineralogy, micropaleontology, and geochemistry, on a sediment core from the outer shelf of the East China Sea (ECS). The identification of greigite and pyrite is first documented, and then the paleoenvironmental implications are evaluated.

2. General Setting and Material

2.1. Regional Setting

As a typical marginal sea of the northwestern Pacific, the ECS is mainly composed of a continental shelf area (<200 m water depth) and the Okinawa Trough (>200 m water depth) (Figure 1a) (Qin et al., 1987). The ECS has a total area of 773,000 km², and ~2/3 of this area is occupied by the continental shelf, which is one of the broadest shelves in the world and is usually divided geomorphologically into the inner and outer shelf by the 50–60 m isobath (Liu et al., 2000). Because of its large width (around 400–500 km), low gradient (<0.02° on average), and relatively shallow water depths (generally < 130 m), the shelf is highly sensitive to sea-level change (Xu et al., 2020). It has received a large quantity of terrigenous matter in response to the high level of sediment discharge from the Yangtze River and sufficient accommodation space due to the high subsidence rates of ~300 m/Myr during the Quaternary (Berné et al., 2002).

The oceanic circulation of the ECS primarily consists of the northward Kuroshio Current (KC) with high temperature and salinity and the Taiwan Warm Current (TWC) with high nutrient content, but low dissolved oxygen, and the low-temperature and low-salinity Zhejiang-Fujian Coastal Current (ZFCC) flowing southwards in winter and northwards in summer (Figure 1a) (Guan, 1983). With the transportation of stronger ZFCC in winter and the obstruction of the TWC, the suspended Yangtze sediments are mainly captured on the inner shelf, resulting in the mud deposits off the Zhe-Min coast (Figure 1b) (Li et al., 2014). Another hydrodynamic feature is the Pacific tidal wave that intrudes into the ECS through the straits among the Ryukyu Islands basically in reciprocating currents (Fang, 1994). This feature had a great influence on the sedimentary processes on the outer shelf during Quaternary transgressions, which is indicated by the multiperiod tidal sand ridges with an NW-SE strike, consistent with the primary tidal current direction (Figure 1b) (Liu et al., 2003).

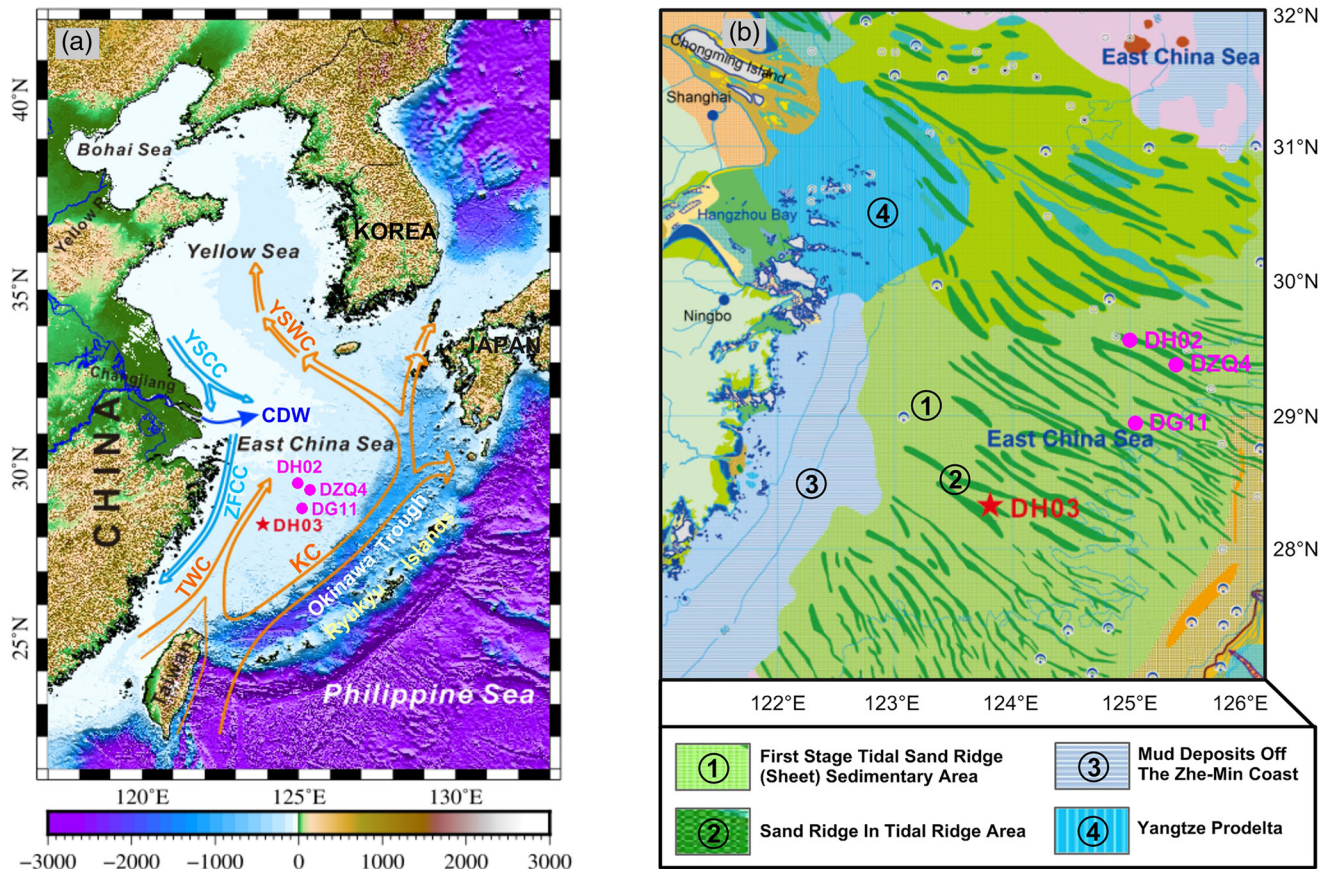


Figure 1. Location of the studied core (DH03, star) and other cores (solid circles) mentioned in the text. (a) Schematic map of the marginal seas of the northwest Pacific with the major oceanic circulations. (b) Sedimentary environment map of the seafloor of the East China Sea (modified after Li et al., 2014). Cores DZQ4, DG11, and DH02 are from Liu et al. (2000), Berné et al. (2002), and Xu et al. (2020), respectively. The abbreviations of oceanic circulations in (a) denote the Kuroshio Current, KC; Taiwan Warm Current, TWC; Yellow Sea Warm Current, YSWC; Yellow Sea Coastal Current, YSCC; Zhejiang-Fujian Coastal Current, ZFCC; and Changjiang Diluted Water, CDW.

2.2. Core Description and Chronology

The studied sediment core, DH03 (123°48'E, 28°18'N), was recovered from the tidal sand area on the outer shelf of the ECS at a water depth of 96 m (Figure 1). It was recovered using the rotary drilling method in September 2015, with a total drilling length of 101.6 m and an average recovery rate of 81.56%. According to core descriptions and grain-size analysis, using the same methods as Xu et al. (2020) employed on core DH02 (Figure 1), fine sand dominates the upper ~48-m section of the core, while clayey silt, sandy silt or fine sand alternately dominates the lower ~53-m section (Figure 2a). The chronology of core DH03 was established by integrating accelerator mass spectrometer (AMS) ^{14}C ages of epibenthic foraminiferal tests measured by Beta Analytic Inc. (Table 1; see Liu et al., 2010 for the details of calibration), microfossil analysis (see Xu et al., 2020 for the methods followed), sedimentary features, and the chronostratigraphy of cores DZQ4 (Liu et al., 2000) and DH02 (Xu et al., 2020) (Figure 1), as outlined below.

The AMS ^{14}C ages of the upper 44-m section are relatively young (~3 kyr) with obvious stratigraphic reversals (Figure 2a and Table 1), just as reported for core DG11 (Figure 1), which indicates that these tidal sand ridges probably formed around 2–3 kyr BP, or they are still in equilibrium with the modern hydrodynamic regime after their initial formation during the last deglacial transgression (Berné et al., 2002; Xu et al., 2020). The BF of the 21–32-m and 44–48-m sections are dominated by relict crusts (Figure 2d), but sedimentary features of the lower section are more consistent with a fluvial setting (Figure S1). In contrast, the values of the AMS ^{14}C ages below 48 m yield ~30,000–40,000 cal yr BP and increase with depth with no stratigraphic reversals (Figure 2a and Table 1), indicating high reliability of these ages. Therefore, although

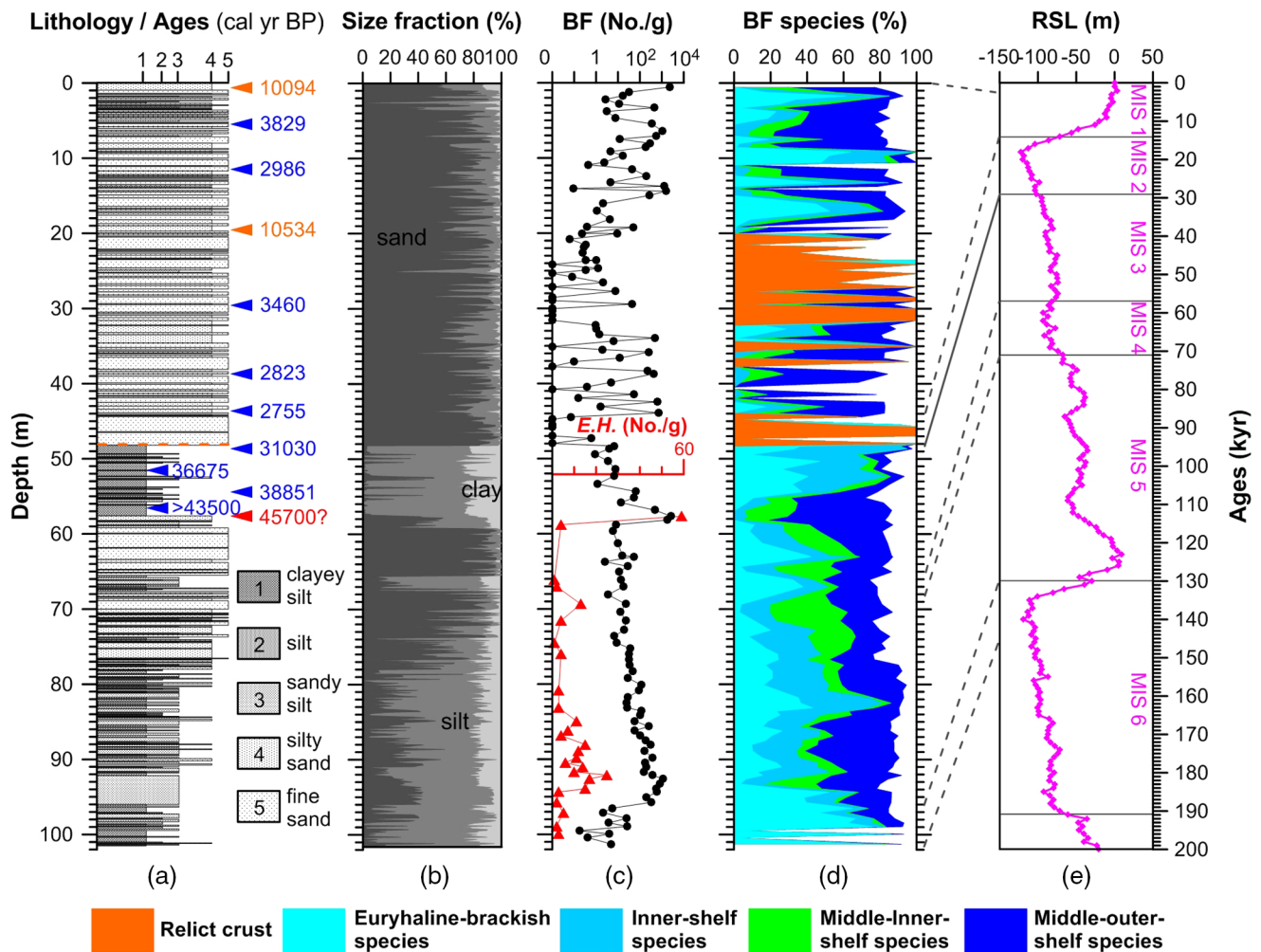


Figure 2. Scheme of the chronostratigraphic reconstruction for core DH03. (a) Variations in lithology, (b) grain-size fraction percentage, (c) benthic foraminifera (BF, the black dots) and *Emiliana huxleyi* (*E.H.*, the red triangles; one kind of calcareous nannofossil) abundance, (d) the percentages of different BF species along the depth of core DH03, and (e) the global relative sea-level (RSL; Rohling et al., 2014). The orange and blue colored numbers in (a) denote AMS¹⁴C ages from bivalve shell and benthic foraminifera, respectively, the red is from a calcareous nannofossil analysis, and the orange colored dash line indicates a possible sedimentary hiatus.

there should be a large sedimentary hiatus at ~48 m, apparently associated with a lithological change (Figure 2a), a terrestrial interval (i.e., 44–48 m) is confirmed to have been deposited after the MIS 3, most probably during the Last Glacial Maximum (LGM) when the sea-level fell by almost 150 m relative to the present in the ECS (Li et al., 2014).

A calcareous nannofossil-derived age was presumed at 57.67 m (Figure 2c), based on the fact that the *Emiliana huxleyi* (*E.H.*) Acme Zone began at ~45.7 kyr BP in shallow marginal seas (Incarbona et al., 2009). According to a linear extrapolation of the sedimentation rates coupled with the assertion that tidal sand ridges had developed during the early MIS 3 transgression (Liu et al., 2000), the base of the MIS 3 stratum in the studied core was estimated to be at ~65 m (Figure 2). In addition, Liu et al. (2000) suggested that the MIS 4 stratum in core DZQ 4 (Figure 1) represents a thin layer of clayey silt, which may correspond to the ~65–68-m interval in core DH03 (Figure 2). Furthermore, the remarkably low abundance of BF that are dominated by shallow-water species at the bottom indicates that the studied core is likely to include MIS 6 deposits (Figure 2). Hereon, this work will focus on the ~44–58-m interval with a robust chronology and a regular profile of magnetic mineral variations (see below).

Table 1
Detailed Information of AMS ^{14}C Ages From Core DH03

Depth (m)	Material	Species	$\delta^{13}\text{C}$ (‰)	Conventional ^{14}C age (yr BP)	Calibrated age (cal yr BP)		Lab no. (Beta)
					Intercept	Range (1 σ)	
0.74	Bivalve shell	<i>Pecten albicans</i>	+1.0	9,180 \pm 30	10,094	10,006–10,195	
5.47	Foraminifera	<i>Pseudorotalia indopacifica</i> , <i>Rotalinoides compressiuscula</i> , <i>Lenticulina</i> sp.	+0.3	3,770 \pm 30	3,829	3,722–3,916	459494
11.45	Foraminifera	<i>Pseudorotalia indopacifica</i> , <i>Rotalinoides compressiuscula</i> , <i>Quinqueloculina bicostata</i>	+0.1	3,090 \pm 30	2,986	2,878–3,072	466866
19.20	Bivalve shell	<i>Veneridae</i> or <i>Crassatellidae</i> ?	+1.1	9,550 \pm 30	10,534	10,455–10,630	466867
29.40	Foraminifera	<i>Pseudorotalia indopacifica</i> , <i>Rotalinoides compressiuscula</i>	−0.1	3,470 \pm 30	3,460	3,380–3,539	466868
38.70	Foraminifera	<i>Pseudorotalia indopacifica</i>	+0.6	2,950 \pm 30	2,823	2,741–2,881	466869
43.81	Foraminifera	<i>Pseudorotalia indopacifica</i> , <i>Lenticulina</i> sp.	+0.6	2,880 \pm 30	2,755	2,696–2,826	517586
48.50	Foraminifera	<i>Quinqueloculina lamarckiana</i> , <i>Rotalinoides compressiuscula</i>	−0.6	27,260 \pm 120	31,030	30,930–31,133	517585
51.40	Foraminifera	<i>Quinqueloculina lamarckiana</i> , <i>Rotalinoides compressiuscula</i>	+0.1	33,040 \pm 200	36,675	36,327–36,931	531778
54.37	Foraminifera	<i>Quinqueloculina lamarckiana</i> , <i>Rotalinoides compressiuscula</i>	−0.8	34,670 \pm 220	38,851	38,574–39,080	524847
55.40	Foraminifera	<i>Quinqueloculina lamarckiana</i> , <i>Rotalinoides compressiuscula</i>	+0.2	35,890 \pm 280	40,202	39,827–40,529	581626
56.40	Foraminifera	<i>Rotalinoides compressiuscula</i> , <i>Heterolepa dutemplei</i>	+0.3	>43,500			531779
58.37	Foraminifera	<i>Pseudorotalia indopacifica</i> , <i>Lenticulina</i> sp.	+0.6	>43,500			523049

Abbreviation: AMS, accelerator mass spectrometer.

3. Methods

3.1. Rock Magnetism

A total of 121 hysteresis loops were measured at stratigraphic intervals of 0.5–1 m using a Princeton Measurement Corporation vibrating sample magnetometer (VSM 3900) in a field cycle between ± 1.5 T, with a 5-mT field increment and an averaging time of 300 ms. Coercivity (B_c), saturation remanence (M_{rs}), and saturation magnetization (M_s) were determined after paramagnetic corrections with an assumed saturating field of 0.5 T for most of the measured hysteresis loops (see Figure S2). Backfields up to ~ 100 mT were applied subsequently to obtain the coercivity of remanence (B_{cr}). For five representative samples, 100 first-order reversal curves (FORCs) were also measured at a maximum field of 1.5 T and an averaging time of 500 ms using the VSM 3900. The corresponding FORC diagrams (Pike et al., 1999) were then processed by the FORCinel software (v1.18; Harrison & Feinberg, 2008) with a smoothing factor of 5.

Magnetic susceptibility (MS, χ , mass-specific) was measured on a total of 737 samples that were collected at ~ 0.1 -m intervals using a MFK1-FA Kappabridge (Agico Ltd, Brno). S ratios were also measured at the same depths where the MS was measured. Specifically, a 1-T field was first applied to impart an isothermal remanent magnetization (IRM), which is regarded as the saturation IRM (SIRM), and then a 0.3-T backfield was applied to impart the $\text{IRM}_{0.3\text{T}}$. The S-ratio is defined as $(1 - \text{IRM}_{0.3\text{T}}/\text{SIRM})/2$ (Bloemendahl et al., 1992). Thermal demagnetization (TD) of three-axis IRM (Lowrie, 1990) and low-temperature (LT) measurements were also conducted on the representative samples for which the FORCs were measured. For the TD of three-axis IRM, the specimens were magnetized successively by induced fields of 1.5, 0.15, and 0.05 T along three orthogonal axes, (i.e., the z-, y-, and x-axis, respectively) which were then demagnetized thermally from room temperature to 690°C at heating intervals of 20–50°C. The LT curves were measured using a Quantum Design Magnetic Property Measurement System (MPMS; model XL5) by cooling the specimens to 20 K in a zero magnetic field first, then exerting a 2.5-T field to impart an IRM, and finally sweeping the temperature up to 300 K at a heating rate of 5 K/min in a zero field. These magnetic measurements were undertaken at the Paleomagnetism and Geochronology Laboratory, Institute of Geology and Geophysics, Chinese Academy of Sciences (IGG-CAS) in Beijing.

3.2. Microscopy and Geochemistry

Scanning electron microscope (SEM) and transmission electron microscope (TEM) observations of bulk sediments and magnetic extracts were conducted at the Electron Microscope Laboratory, IGG-CAS. Magnetic minerals were extracted following Zhang et al. (2018). SEM observations were made with a FEI Apreo field emission SEM. Magnetic extracts or bulk sediments were fixed onto an aluminum SEM stub using copper tape and then coated with carbon. Backscattered electron images were acquired at 5 kV. The TEM analyses on magnetic extracts were also conducted following Zhang et al. (2018). The elemental compositions of typical particles were found by energy-dispersive X-ray spectroscopy (EDXS) analysis. Total organic carbon (TOC) and major elements, including Fe and S, were measured using samples of homogenous lithology from the focused layer at the Key Laboratory of Marine Geology and Metallogeny, Ministry of Natural Resources (MNR). The experimental procedures for these analyses can be found in Wu et al. (2020) and Zhang et al. (2020), respectively.

4. Results

4.1. Rock Magnetism

Hysteresis results show that most of the measured sediments have B_c values less than 20 mT, indicating magnetic dominance of low-coercivity minerals (e.g., magnetite), whereas sediments from the ~48–52-m interval possess much higher B_c values (>40 mT; Figure 3a), with relatively uniform B_{cr}/B_c and M_{rs}/M_s ratios of ~1.5 and ~0.5, respectively (Figures 3b–3c). They also show higher SIRM/ χ ratios (Figure 3d), which implies possible enrichment of greigite within this interval (Roberts, 1995). The ~52–54.5-m interval shows intermediate values for B_c , B_{cr}/B_c , M_{rs}/M_s , SIRM/ χ , and S-ratio between those of the ~48–52-m and ~54.5–58-m intervals, while the upper ~44–48-m interval also possesses different values of these rock magnetic parameters from the lower three intervals (Figure 3). These results indicate that the ~44–58-m stratigraphic interval bears regular variations in magnetic minerals. It therefore can be divided into four units, namely Unit 1 to Unit 4 in ascending order, which are assigned roughly to the middle MIS 3, the middle-late MIS 3, the late MIS 3, and the LGM deposits, respectively (Figure 3), according to the reconstructed chronology (Figure 2 and Table 1).

The FORC diagrams for samples from Unit 3 show typical single domain (SD) magnetic properties as indicated by the closed concentric contours about a central peak where the B_c values are 60–70 mT (Figures 4c2–4c3), which is also probably indicative of SD greigite (Roberts et al., 2006). Except for an obvious SD component similar to that of Unit 3, the FORC diagrams for Unit 2 also indicate another SD component with a peak B_c value of ~20 mT (Figure 4c4). In contrast, sediments from Units 4 and 1 are magnetically dominated by vortex-state (see Roberts et al., 2017 for why this term is more relevant than “pseudo-single domain” (PSD) that has been used conventionally) to multidomain (MD) particles (Roberts et al., 2014), with a minor presence of SD particles of which the peak B_c is ~12 mT (Figures 4c1 and 4c5). Also, there are still some vortex-state to MD particles in sediments from Units 3 and 2, as indicated by the diverging contours in the FORC diagrams (Figures 4c2–4c4). These observations are also consistent with the corresponding Day plot (Figure S3; Dunlop, 2002a, 2002b), which increases the likelihood of greigite enrichment in Unit 3, since it commonly occurs in a SD state in natural environments (Roberts et al., 2011).

The temperature-dependent measurements provide more robust clues to the rock magnetic diagnosis. For samples from Units 3 and 2, the TD of three-axis IRM reveals a dominant medium-coercivity IRM fraction that drops significantly between 240°C and 360°C (Figures 4d2–4d4) where greigite undergoes chemical decomposition (Chang et al., 2008). However, sediments in Unit 2 contain a higher percentage of magnetic components that have maximum unblocking temperatures of ~580°C and ~680°C (i.e., the Curie/Néel temperatures of magnetite and hematite, respectively; Dunlop & Özdemir, 1997) than those in Unit 3 (Figures 4d2–4d4). In addition to a dominant low-coercivity IRM mainly unblocking below 600°C, samples from Unit 1 with extremely low saturation SIRM (Figure 4b) have a higher relative content of medium-to-high-coercivity fractions, of which IRMs unblock completely up to ~680°C (Figure 4d5), the Néel temperature of hematite (Dunlop & Özdemir, 1997). An observable decrease in the low- and medium-coercivity IRM fractions at ~360°C should indicate trace amounts of greigite in the sediments of Unit 1 (Figure 4d5).

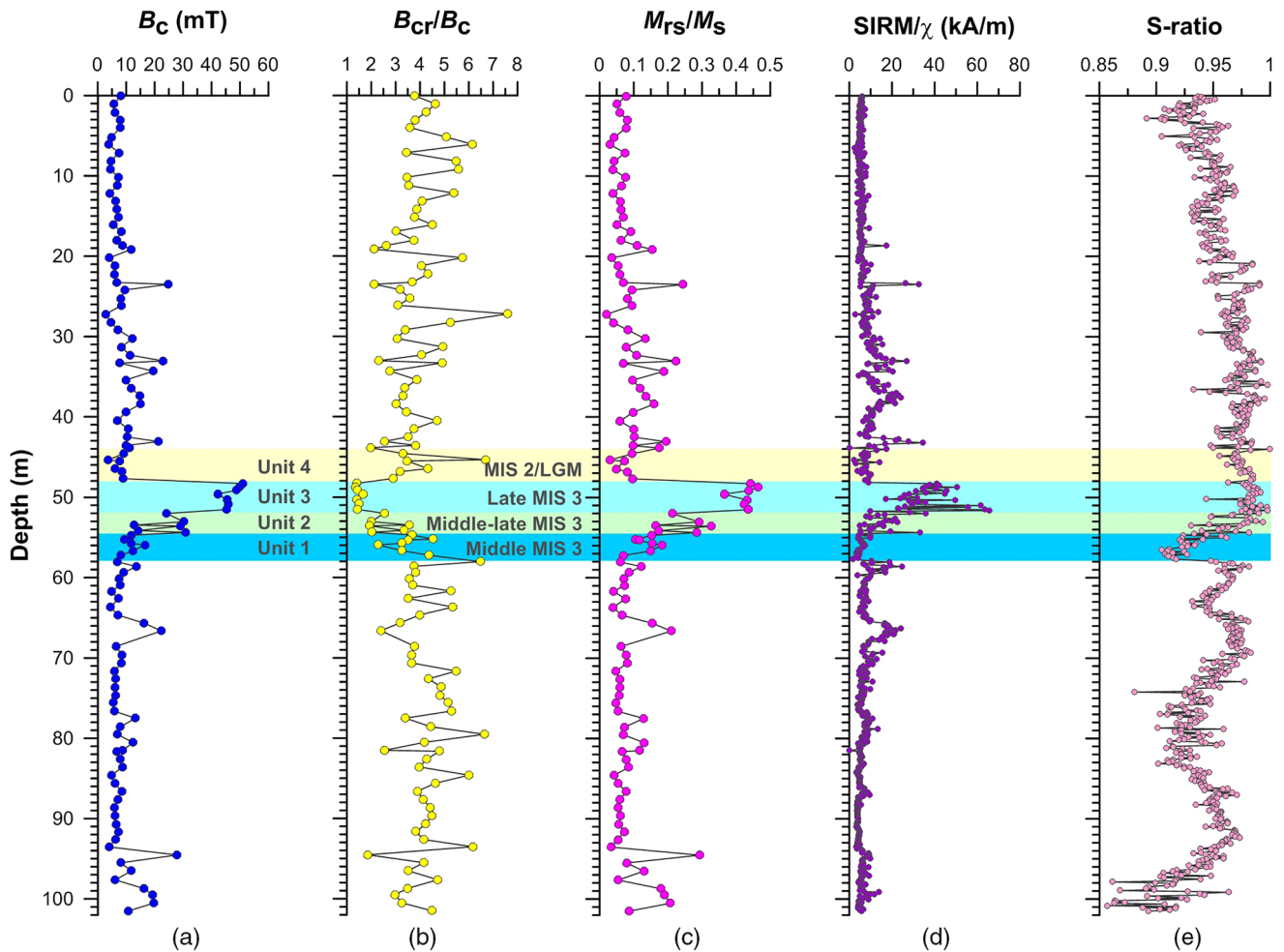


Figure 3. Variations in the magnetic parameters versus depth along core DH03. (a) Coercivity (B_c), (b) ratios of coercivity of remanence (B_{cr}) to B_c , (c) saturation remanence (M_{rs}) to saturation magnetization (M_s), (d) saturation isothermal remanent magnetization (SIRM) to mass-specific magnetic susceptibility (χ), and (e) S-ratio, defined as $(1 - \text{IRM}_{0.3T} / \text{SIRM}) / 2$ (Bloemendahl et al., 1992), where SIRM and $\text{IRM}_{0.3T}$ denote the isothermal remanent magnetizations imparted successively by a 1-T field and 0.3-T backfield. Data for the 0–48-m interval in (a) and (d) are partly from Liu et al. (2020).

Samples from Unit 4 are magnetically dominated by low-coercivity minerals unblocking at $\sim 580^\circ\text{C}$, the Curie temperature of magnetite. The remaining medium-coercivity IRM at temperatures higher than 580°C and the high-coercivity IRM fully unblock at $\sim 680^\circ\text{C}$ (Figure 4g), which is indicative of a minor contribution of hematite (Dunlop & Özdemir, 1997).

The Verwey transition (Verwey, 1939) is detected in all measured samples on the LT curves at 110–120 K (Figures 4e2–4e5), indicating the presence of detrital magnetite rather than biogenic magnetite (Chang et al., 2016). Moreover, the absence of the Besnus transition between 30–34 K can exclude the presence of monoclinic pyrrhotite (Fe_7S_8) in high proportions in the studied sediments (Rochette et al., 1990), which, however, is unable to exclude sedimentary hexagonal pyrrhotite that also lacks a LT magnetic transition, as does greigite (Horng, 2018).

4.2. Microscopy and Geochemistry

SEM images of both magnetic extracts (Figures 5a–5d) and bulk sediments (Figures 5e–5h) reveal magnetic particles with grain sizes ranging from tens of nanometers to several microns. The corresponding EDXS results indicate that the smaller particles are dominant in Fe and S (Figures 5n and 5p), and the larger ones

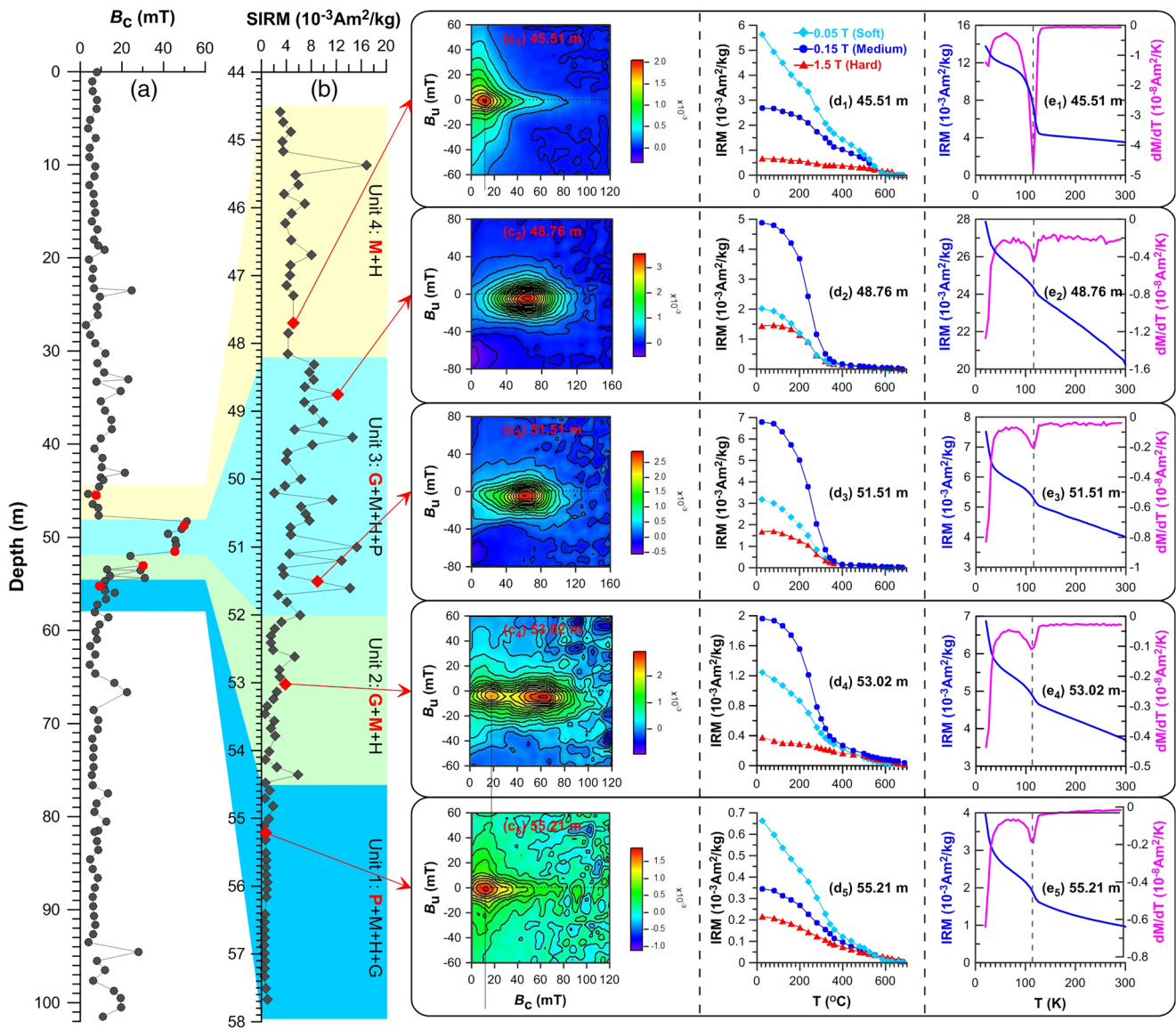


Figure 4. Rock magnetic results for the ~44–58-m stratigraphic interval of core DH03. (a) Coercivity (B_c) and saturation isothermal remanent magnetization (SIRM), (c_1 – c_5) first-order reversal curve (FORC) diagrams, (d_1 – d_5) thermal demagnetization of three-axis IRMs, and (e_1 – e_5) low-temperature (20–300-K) isothermal remanent magnetization (2.5-T) warming curves for representative samples, with the first derivatives of the IRM with respect to temperature ($d\text{IRM}/dT$) plotted on the right-hand y-axis to emphasize the possible magnetic transitions during warming. The red-colored symbols in (a) and (b) denote the representative samples on which the detailed rock magnetic analyses were conducted, and the abbreviations G, M, H, and P in (b) denote greigite, magnetite, hematite, and pyrite, respectively, while bold red font indicates the dominant magnetic components in each unit.

are dominant in Fe and O (Figure 5o). In contrast to the magnetic extracts which are mainly ferrimagnetic, the magnetic particles in the bulk sediments appear as octahedrons (Figures 5e–5h) and have much higher ratios of S to Fe (Figure 5p), closer to that of pyrite, and also have a higher electron backscatter due to the smoother surfaces of the coarser pyrite grains than those of fine-grained greigite with less regular surfaces (Roberts & Weaver, 2005). TEM images of magnetic extracts (Figures 5i–5j, 5l) indicate that the magnetic particles that are exceptionally rich in Fe and S (Figure 5q) generally have grain sizes below the upper threshold values (~500 nm) for octahedral crystals of SD greigite (Roberts et al., 2011), also consistent with the Day plot (Figure S3) and FORC diagrams (Figures 4c2–4c3). Furthermore, the strong diffraction patterns (Figures 5k and 5m) revealed by selected-area electron diffraction (SAED) indicate good crystallinity, with values of the corresponding Miller indices (hkl) matching well with those of greigite. These observations

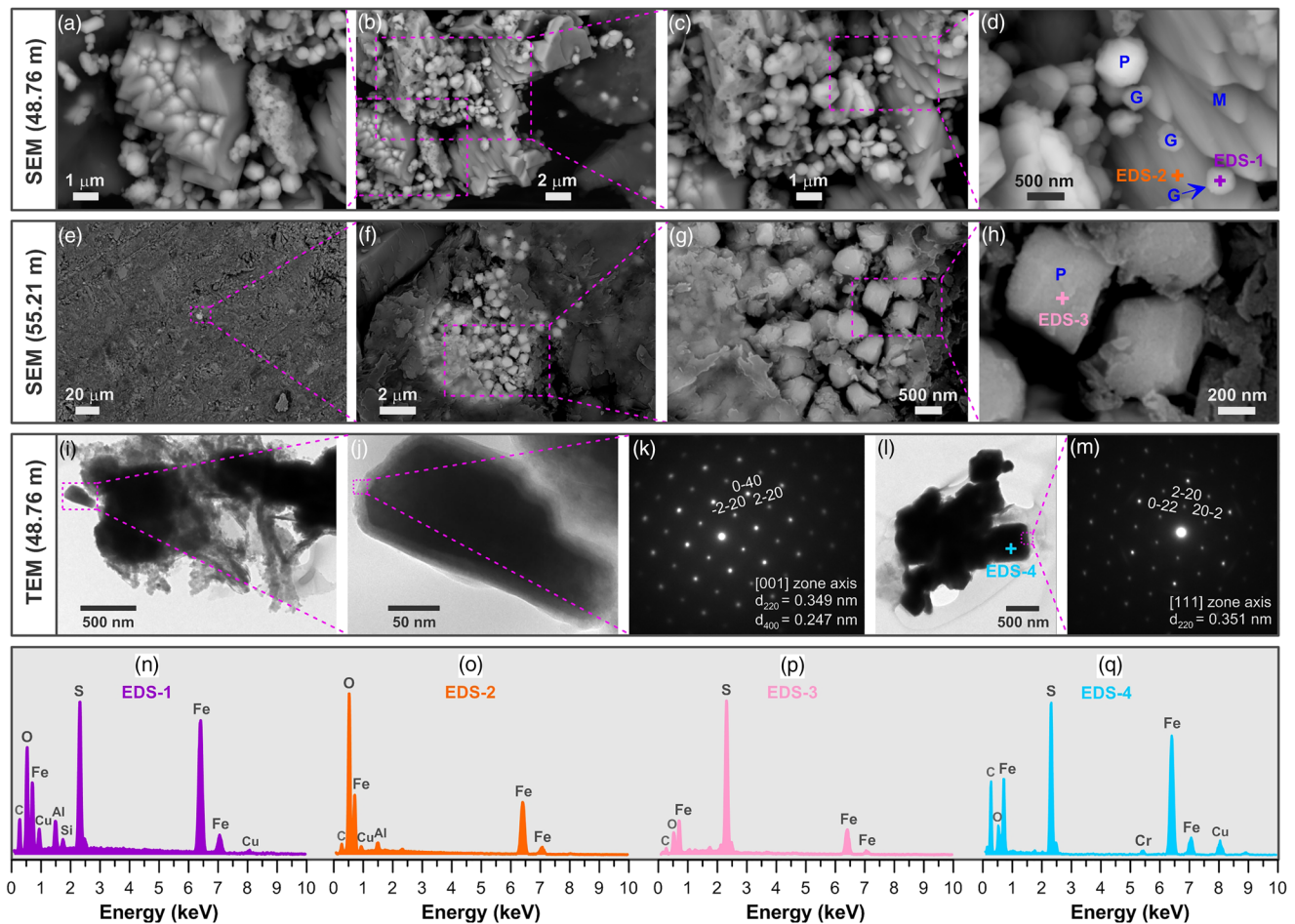


Figure 5. Electron microscopy results of the representative samples. (a–d) Representative back-scattered SEM images of magnetic extracts, (e–h) bulk sediments, (i, j, l) TEM images and the associated (k, m) selected area electron diffraction (SAED) patterns of magnetic extracts, (n–q) Energy-dispersive X-ray spectroscopy (EDS) of magnetic particles labeled in the SEM and TEM images. The abbreviations G, M, and P in (d) and (h) denote greigite, magnetite, and pyrite, respectively. SEM, Scanning electron microscope; TEM, transmission electron microscope.

coupled with the FORC diagrams (Figures 4c2–4c4) and the TD of three-axis IRM (Figures 4d2–4d4) can demonstrably exclude the presence of sedimentary hexagonal pyrrhotite, which has a Curie temperature of ~320°C and higher coercivities than greigite (Hornig, 2018).

To avoid grain-size effect, only geochemical results of fine-grained sediments were used in this study (Figure 6a). Total iron, expressed as TFe₂O₃, ranges from 5.25% to 6.24%, generally with a downcore descending tendency. The TOC and S contents have ranges of 0.42–0.91% and 627–2,145 ppm, respectively, and the former decreases slightly with depth, while the latter increases downwards (Figure 6c).

4.3. Rock Magnetic Summary and Paleoenvironmental Zonations

Based on the rock magnetic and electron microscope analyses, the magnetic mineral assemblages in Units 1 to 4 are further evaluated (Figures 4b and 6a). Unit 1 that is enriched in pyrite is proportionally rich in coarser vortex-state and MD magnetite grains, and high-coercivity minerals such as hematite, with a smaller quantity of greigite, according to the following lines of evidence: (1) the lowest S-ratio (Figure 3e) and SIRM values (Figure 4b) indicate the highest relative content of high-coercivity minerals (Bloemendal et al., 1992), and the lowest magnetic mineral concentration (Liu et al., 2012), respectively; (2) the vortex-state to MD magnetic properties revealed by the FORC diagrams (Figure 4c5) and Day plot (Figure S3); (3) the dominant

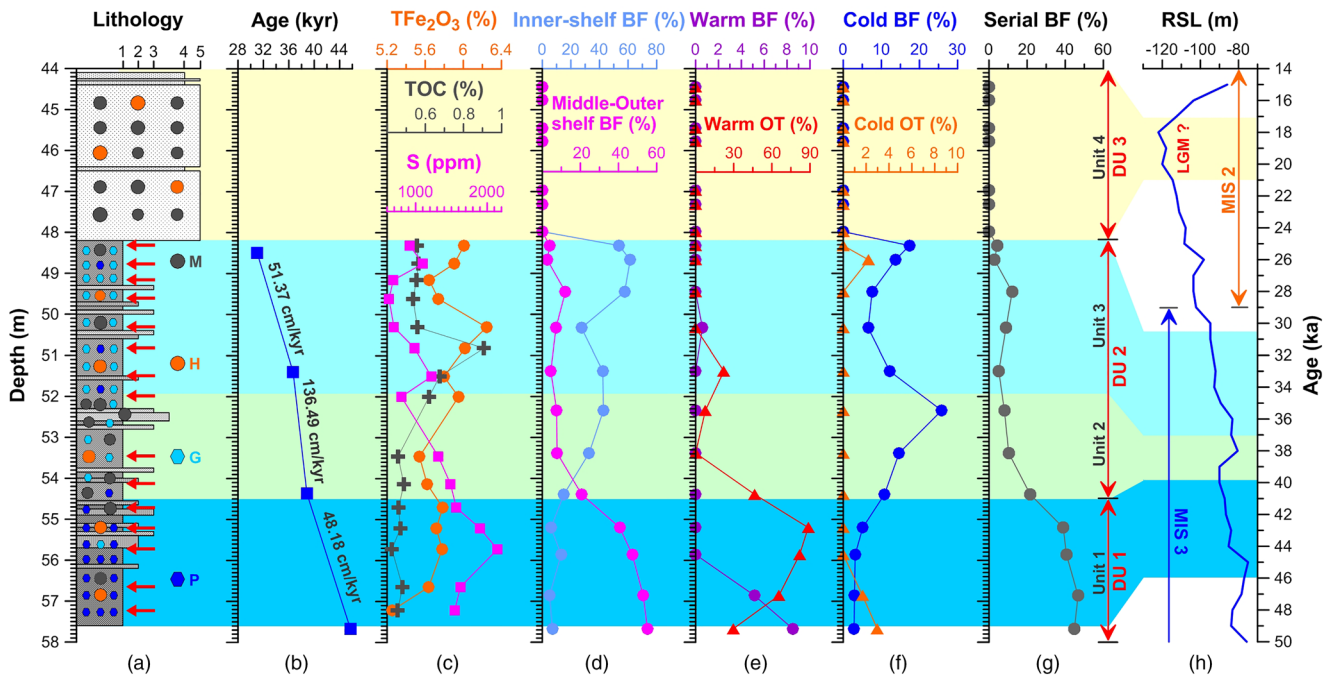


Figure 6. Paleoenvironmental and rock magnetic zonations of the interval of interest (i.e., ~44–58-m) in the studied core DH03. (a) Lithology with a diagrammatic sketch of magnetic mineral assemblages (legends and abbreviations are the same as for Figures 2a and 4b, respectively), (b) age–depth relationship with sedimentation rates indicated, (c) variations of total iron expressed as TFe_2O_3 (orange circles), TOC (gray crosses), and sulfur (S, magenta squares), and the relative abundance for (d) inner-shelf (light blue circles) and middle-outer shelf BF species (magenta circles), (e) warm-water species of BF (purple circles) and ostracods (OT, red triangles), (f) cold-water species of BF (blue circles) and OT (orange triangles), and (g) serial BF species that are low-oxygen tolerant and nutrient favorite. (j) The global relative sea-level (RSL, Rohling et al., 2014). The red arrows in (a) indicate the stratigraphic levels where geochemical analyses were done.

contributions of magnetic minerals of which IRMs fully unblock at $\sim 580^\circ\text{C}$ and 680°C , respectively, to remanence, with an observable drop of low- and medium-coercivity IRM fractions at $\sim 360^\circ\text{C}$ (Figure 4d5), and the strong Verwey transition on the LT curves (Figure 4e5); (4) the facts that coarser magnetite grains react more slowly with dissolved sulfide due to the smaller surface area to volume ratios, and that hematite is more resistant to dissolution than magnetite in sulfidic environments (Rowan et al., 2009); and (5) that it is relatively easy to observe pyrite under SEM in the bulk sediments (Figures 5e–5h). In addition to greigite, Unit 2 also contains considerable amount of magnetite with some hematite, which may have resulted from limited porewater sulfate due to an accelerated sedimentation rate within this unit (Figure 6b), as reported in Argentinian margin sediments (Riedinger et al., 2005). In contrast, Unit 3 is dominated magnetically by greigite with some magnetite and hematite and trace of pyrite. Whereas the magnetic minerals in Unit 4 are dominated by magnetite with some hematite.

According to the microfossil analyses, the focused stratigraphic interval (i.e., ~44–58-m interval) can be divided into three depositional units (DUs), namely DU 1 to DU 3 in ascending order (Figure 6 and Figure S4). Both BF and ostracods in DU 1 (~54.5–58 m, corresponding to Unit 1) are dominated by middle-outer shelf species (Figure 6d and Figures S4g–S4h), with high numbers of warm-water species (Figure 6e and Figures S4i–S4j), indicating a middle-outer shelf setting with a strong warm current (i.e., the TWC). DU 1 is also rich in serial species of BF (Figure 6g), mainly *Bolivina robusta*, *Bulimina marginata*, and *Cassidulina laevigata* (Table S1), which are typical of low-oxygen and eutrophic bottom-waters caused by enhanced upwelling (Usami et al., 2013; Wang et al., 2014). In contrast, BF and ostracods in DU 2 (~48–54.5 m, covering Units 2 and 3) are dominated by inner-shelf species (Figure 6d and Figures S4c–S4d), with a higher percentage of euryhaline-brackish species (Figures S4a–S4b). It is also rich in cold-water species of BF (Figure 6f), mainly *Protelphidium tuberculatum* and *Buccella frigida* (Table S1). These results indicate that DU 2 was deposited in a prodelta setting and was affected by cold coastal currents (Xu et al., 2020). DU 3 (~44–48 m, corresponding to Unit 4), as above-mentioned, was deposited in a terrestrial setting, as indicated by both

the sedimentary features (Figure S1) and the extremely low abundance of BF that are dominated by relict crust (Figures 2c–2d).

5. Discussion

Although greigite can form at any time when dissolved iron and sulfide are available during diagenesis (Roberts et al., 2011), its formation during later diagenesis is often related to the potential mobility of methane via fracture and fault networks in tectonically active settings (Larrasoana et al., 2007; Roberts, 2015). Moreover, recent studies have demonstrated that the peak values of sulfate reduction rates (SRRs) are usually reached near the sediment-water interface in shallow-water environments, such as the inner and outer shelves (Bowles et al., 2014), and that most pyrite framboids are formed during the earliest stages of diagenesis, mainly within about 5 years after the deposition of its host sediments (Rickard, 2019). In addition, the subsurface sulfate reduction maxima (i.e., the peak SRRs) have always been observed at depths of 5–15 cm below the seafloor in the ECS continental shelf sediments (Huang & Lin, 1995). These lines of evidence, coupled with the facts that the ECS shelf basin has undergone stable subsidence since the Quaternary (Qin et al., 1987) and that hydrocarbon seepage has not been reported at such shallow depths, collectively suggest that the identified iron sulfides in core DH03 formed via organoclastic sulfate reduction more or less syn-depositionally. Thus, they can be taken as credible recorders of environmental evolution.

It is evident that there is a strong correlation between the dominant iron-bearing mineral variations (i.e., pyrite→greigite→magnetite from Units 1 to 4) and sea-level change from the middle MIS 3 to the LGM (Figure 6). Nonsteady state diagenesis (see Roberts, 2015 for the nomenclature) induced by variations in pore-fluid migration (e.g., Oda & Torri, 2004), sedimentation rate (e.g., Zheng et al., 2010), or organic carbon and sulfate supply (e.g., Liu et al., 2005; Wang et al., 2015), has been invoked to interpret the formation and preservation of authigenic greigite and its end-product, pyrite, in continental shelf sediments. Essentially, these conditions are controlled largely by sea-level change. For example, greigite was discovered to prevail more in the lower section of a postglacial (~13 kyr BP) record from the southeastern South Yellow Sea (SYS) than in the corresponding upper section (Liu et al., 2005). This was attributed to the deposition of the upper section in a cold-eddy environment associated with the Yellow Sea Warm Current (YSWC, Figure 1a) after the middle-Holocene (~6 kyr BP) maximum sea-level, and therefore in more reductive conditions favorable for complete pyritization (Liu et al., 2005). Similarly, the MIS 17–13 sediments from the central SYS muddy area are magnetically dominated by greigite, while the underlying MIS 21–19 sediments, when the YSWC and associated YS Cold Water Mass were stronger due to higher sea level, are richer in pyrite (Liu et al., 2018).

The pyrite enrichment in Unit 1 indicates a strong reductive environment, with much higher sulfur contents (Figure 6c), which usually indicates strong sulfidic conditions (Shi et al., 2016). This could be caused by enhanced upwelling due to the TWC development when sea-level was relatively high, since the TWC generally flows along the 50–100-m isobath (Hu, 1984). The greigite enrichment in the subsequent Units 2 and 3 may be the result of a limitation of sulfate coupled with a higher detrital iron supply (Figure 6c) following an environmental transition from marine to terrestrial settings in response to sea-level falling from the late MIS 3 to the LGM (Figure 6). It has been demonstrated that greigite preservation is favored when the supply of H₂S is deficient relative to Fe²⁺ (Kao et al., 2004; Rowan & Roberts, 2006). A similar case was reported in the Yellow River delta of the Bohai Sea, where greigite was enriched at a transition zone between shallow marine and lacustrine facies because of a limited supply of sulfate (Wang et al., 2015). In contrast, greigite enrichment in the SYS sediments has been interpreted to be the result of limited organic matter supply due to a moderate level of primary productivity, which has limited sulfate reduction, and so constrained the availability of sulfide for greigite to pyrite conversion (Liu et al., 2018). In any case, both sulfate and organic matter supplies are regulated by sea-level change, which controls the oceanic circulation modes and associated sedimentation at least in the marginal seas east of China (Hu, 1984).

As mentioned above, Unit 3 is dominated magnetically by greigite and is assigned to prodelta deposits based on the microfossil analyses (Figure 6). In general, the prodelta facies develops below the wave-base, which is typically at water depths of ~20 m in the marginal seas east of China and represents the distal part of deltas. Those derived from the paleo-Yangtze River in the late MIS 3 have been reported widely (e.g., Berné

et al., 2002; Saito et al., 1998; Xu et al., 2018). The corresponding water depth of the prodelta has been proposed to be ~15–30 m in the Yangtze River delta (Xu et al., 2016), while Huang et al. (1996) suggest a maximum value of ~30 m for the eastern boundary of the prodelta facies in the north and ~60 m for the exterior margin in the southeast. Unit 3 has higher percentages of inner-shelf species of BF and ostracods but lower euryhaline-brackish ones (Figure S3) than the northern cores (e.g., Xu et al., 2018), implying greater water depths. Based on these facts and the global sea-level curve (Figure 6h, Rohling et al., 2014), regardless of local tectonics and sediment compaction, a paleo-water depth range of ~50–60 m is evaluated for Unit 3. Likewise, estimates of 30–60 m, 45–55 m, and 55–60 m are proposed for the greigite-enriched intervals in the cores from the southeastern SYS (Liu et al., 2005), the Yellow River delta (Wang et al., 2015), and the central SYS muddy area (Liu et al., 2018), respectively. All of these probably suggest a water depth range of 30–60 m is more suitable for extensive greigite preservation in continental shelf sediments while pyrite is more likely to be enriched in water depths >60 m. However, this still needs to be clarified by further studies on continental shelf seas worldwide.

6. Conclusions

We conducted a comprehensive study on a late-Quaternary sediment core from the outer shelf of the ECS, mainly from an environmental magnetic perspective. Systematical rock magnetic studies coupled with electron microscopy analyses reveal authigenic greigite as the major magnetic component in an almost 4-m-thick interval deposited during the late MIS 3. The underlying and overlying sediments are magnetically dominated by pyrite and magnetite, respectively. This implies an upward weakening tendency of reductive conditions. Moreover, microfossil studies, including foraminifera and ostracods analyses, indicate that the profile has undergone successively an environmental variation from a middle-outer shelf setting affected dominantly by the TWC and its derivative upwelling to an inner shelf with prevailing ZFCC, and finally to a fluvial setting, which was regulated essentially by sea-level change from the middle MIS 3 to the LGM. We, therefore, conclude that authigenic greigite and its end-product, pyrite, have great potential as a means of identifying subtle changes in sea-level and paleoceanography of continental shelf seas over relatively short timescales. Additionally, we propose a water depth range of 30–60 m as the extent of the widespread occurrence of authigenic greigite in continental shelf sediments, a finding that warrants further investigation.

Data Availability Statement

The data in this work can be obtained from the Mendeley Data repository at <http://dx.doi.org/10.17632/hfd5j8fbcz.1>.

References

- Berné, S., Vagner, P., Guichard, F., Lericolais, G., Liu, Z. X., Trentesaux, A., et al. (2002). Pleistocene forced regressions and tidal sand ridges in the East China Sea. *Marine Geology*, *188*, 293–315.
- Bloemendal, J., King, J. W., Hall, F. R., & Doh, S.-J. (1992). Rock magnetism of Late Neogene and Pleistocene deep-sea sediments: Relationship to sediment source, diagenetic processes, and sediment lithology. *Journal of Geophysical Research*, *97*, 4361–4375.
- Bowles, M. W., Mogollón, J. M., Kasten, S., Zabel, M., & Hinrichs, K.-U. (2014). Global rates of marine sulfate reduction and implications for sub-sea-floor metabolic activities. *Science*, *344*, 889–891.
- Chang, L., Heslop, D., Roberts, A. P., Rey, D., & Mohamed, K. J. (2016). Discrimination of biogenic and detrital magnetite through a double Verwey transition temperature. *Journal of Geophysical Research: Solid Earth*, *121*, 3–14. <https://doi.org/10.1002/2015JB012485>
- Chang, L., Roberts, A. P., Muxworthy, A. R., Tang, Y., Chen, Q. W., Rowan, C. J., et al. (2007). Magnetic characteristics of synthetic pseudo-single-domain and multi-domain greigite (Fe₃S₄). *Geophysical Research Letters*, *34*, L24304. <https://doi.org/10.1029/2007GL032114>
- Chang, L., Roberts, A. P., Tang, Y., Rainford, B. D., Muxworthy, A. R., & Chen, Q. W. (2008). Fundamental magnetic parameters from pure synthetic greigite (Fe₃S₄). *Journal of Geophysical Research*, *113*, B06104. <https://doi.org/10.1029/2007JB005502>
- Dunlop, D. J. (2002a). Theory and application of the Day plot (M_{rs}/M_s versus H_{cr}/H_c): 1. Theoretical curves and tests using titanomagnetite data. *Journal of Geophysical Research*, *107*, 2056. <https://doi.org/10.1029/2001JB000486>
- Dunlop, D. J. (2002b). Theory and application of the Day plot (M_{rs}/M_s versus H_{cr}/H_c): 2. application to data for rocks, sediments, and soils. *Journal of Geophysical Research*, *107*, 2057. <https://doi.org/10.1029/2001JB000487>
- Dunlop, D. J., & Özdemir, Ö. (1997). *Rock magnetism: Fundamentals and frontiers*. (p. 573). Cambridge, UK: Cambridge University Press. <https://doi.org/10.1017/CBO9780511612794>
- Fang, G. H. (1994). Tides and tidal currents in East China Sea, Huanghai Sea and Bohai Sea. In Zhou, D. (Eds), *Oceanology of China seas* (pp. 101–112). Dordrecht, Kluwer Academic Publisher.

Acknowledgments

The authors kindly thank the crew of the R/V *Kan407* for their help with the core drilling, and Quanhong Zhao (Tongji University) for his assistance in the microfossil analyses. Sincere appreciation is also expressed to Jun Xu, Tengfei Fu, and Yonggui Yu for their assistance with the sampling. This work was jointly supported by the National Natural Science Foundation of China (grants 41976078, 41606075, and U1606401), and the Laboratory for Marine Geology, Qingdao Pilot National Laboratory for Marine Science and Technology (MGQNLMTD201903).

- Fu, Y. Z., Doubeneck, T. V., Franke, C., Heslop, D., & Kasten, S. (2008). Rock magnetic identification and geochemical process models of greigite formation in Quaternary marine sediments from the Gulf of Mexico (IODP Hole U1319A). *Earth and Planetary Science Letters*, 275, 233–245.
- Ge, C., Zhang, W. G., Dong, C. Y., Dong, Y., Bai, X. X., Liu, J. Y., et al. (2015). Magnetic mineral diagenesis in the river-dominated inner shelf of the East China Sea, China. *Journal of Geophysical Research: Solid Earth*, 120, 4720–4733. <https://doi.org/10.1002/2015JB011952>
- Guan, B. X. (1983). Sketch of the current structure and eddy characteristics in the East China Sea. In L., Yuru (Ed.), *Proceedings of the international symposium sedimentation on the continental shelf, with special reference to the East China Sea* (pp. 56–79). Beijing: China Ocean Press (in Chinese).
- Harrison, R. J., & Feinberg, J. M. (2008). FORCinel: An improved algorithm for calculating first-order reversal curve distributions using locally weighted regression smoothing. *Geochemistry, Geophysics, Geosystems*, 9, Q05016. <https://doi.org/10.1029/2008/GC001987>
- Horng, C.-S. (2018). Unusual magnetic properties of sedimentary pyrrhotite in methane seepage sediments: Comparison with metamorphic pyrrhotite and sedimentary greigite. *Journal of Geophysical Research: Solid Earth*, 123, 4601–4617. <https://doi.org/10.1002/2017JB015262>
- Hu, D. X. (1984). Upwelling and sedimentation dynamics I: The role of upwelling in sedimentation in the Yellow Sea and East China Sea—A description of general features. *Chinese Journal of Oceanology and Limnology*, 2, 12–19.
- Huang, H. Z., Tang, B. G., & Yang, W. E. (1996). *Sedimentary geology of the Yangtze delta*, (p. 244). Beijing: China Geological Press. (in Chinese).
- Huang, K.-M., & Lin, S. (1995). The carbon-sulfide-iron relationship and sulfate reduction rate in the East China Sea continental shelf sediments. *Geochemical Journal*, 29, 301–315.
- Incarbona, A., Stefano, E. D., & Bonomo, S. (2009). Calcareous nannofossil biostratigraphy of the central Mediterranean Basin during the last 430,000 years. *Stratigraphy*, 6, 1–12.
- Kao, S.-J., Horng, C.-S., Roberts, A. P., & Liu, K.-K. (2004). Carbon-sulfur-iron relationships in sedimentary rocks from southwestern Taiwan: Influence of geochemical environment on greigite and pyrrhotite formation. *Chemical Geology*, 203, 153–168.
- Larrasoana, J. C., Roberts, A. P., Musgrave, R. J., Gràcia, E., Piñero, E., Vega, M., & Martínez-Ruiz, F. (2007). Diagenetic formation of greigite and pyrrhotite in gas hydrate marine sedimentary systems. *Earth and Planetary Science Letters*, 261, 350–366.
- Li, G. X., Li, P., Liu, Y., Qiao, L. L., Ma, Y. Y., Xu, J. S., & Yang, Z. G. (2014). Sedimentary system response to the global sea level change in the East China Sea since the last glacial maximum. *Earth-Science Reviews*, 139, 390–405.
- Lisiecki, L. E., & Raymo, M. E. (2005). A Pliocene-Pleistocene stack of 57 globally distributed benthic $\delta^{18}\text{O}$ records. *Paleoceanography*, 20, PA1003. <https://doi.org/10.1029/2004PA001071>
- Liu, J., Saito, Y., Kong, X. H., Wang, H., Xiang, L. H., Wen, C., & Nakashima, R. (2010). Sedimentary record of environmental evolution off the Yangtze River estuary, East China Sea, during the last ~13,000 years, with special reference to the influence of the Yellow River on the Yangtze River delta during the last 600 years. *Quaternary Science Reviews*, 29, 2424–2438.
- Liu, J., Zhu, R. X., Li, S. Q., & Chang, J.-H. (2005). Magnetic mineral diagenesis in the post-glacial muddy sediments from the southeastern South Yellow Sea: Response to marine environmental changes. *Science China: Earth Sciences*, 48, 134–144.
- Liu, J., Zhu, R. X., Roberts, A. P., Li, S. Q., & Chang, J.-H. (2004). High-resolution analysis of early diagenetic effects on magnetic minerals in post-middle-Holocene continental shelf sediments from the Korea Strait. *Journal of Geophysical Research: Solid Earth*, 109, B03103. <https://doi.org/10.1029/2003JB002813>
- Liu, J. X., Mei, X., Shi, X. F., Liu, Q. S., Liu, Y. G., & Ge, S. L. (2018). Formation and preservation of greigite (Fe_3S_4) in a thick sediment layer from the central South Yellow Sea. *Geophysical Journal International*, 213, 135–146.
- Liu, J. X., Shi, X. F., Wu, Y. H., Yu, X. X., Shan, X., & Xu, T. Y. (2020). Rock-magnetic properties of thick sandy sediments on the outer continental shelf of East China Sea. *Advances in Marine Science*, 38, 435–445 (in Chinese with English abstract).
- Liu, Q. S., Roberts, A. P., Larrasoana, J. C., Banerjee, S. K., Guyodo, Y., Tauxe, L., & Oldfield, F. (2012). Environmental magnetism: Principles and applications. *Reviews of Geophysics*, 50, RG4002. <https://doi.org/10.1029/2012RG000393>
- Liu, Z. X., Berné, S., Saito, Y., Lericolais, G., & Marsset, T. (2000). Quaternary seismic stratigraphy and paleoenvironments on the continental shelf of the East China Sea. *Journal of Asian Earth Sciences*, 18, 441–452.
- Liu, Z. X., Yin, P., Xiong, Y. Q., Berné, S., Trentesaux, A., & Li, C. X. (2003). Quaternary transgressive and regressive depositional sequences in the East China Sea. *Chinese Science Bulletin*, 48, 81–87.
- Lowrie, W. (1990). Identification of ferromagnetic minerals in a rock by coercivity and unblocking temperature properties. *Geophysical Research Letters*, 17, 159–162.
- Mohamed, K. J., Rey, D., Rubio, B., Dekkers, M. J., Roberts, A. P., & Vilas, F. (2011). Onshore-offshore gradient in reductive early diagenesis in coastal marine sediments of the Ria de Vigo, Northwest Iberian Peninsula. *Continental Shelf Research*, 31, 433–447.
- Nilsson, A., Lee, Y. S., Showball, I., & Hill, M. (2013). Magnetostratigraphic importance of secondary chemical remanent magnetizations carried by greigite (Fe_3S_4) in Miocene sediments, New Jersey shelf (IODP Expedition 313). *Geosphere*, 9, 510–520.
- Oda, H., & Torri, M. (2004). Sea-level change and remagnetization of continental shelf sediments off New Jersey (ODP Leg 174A): Magnetite and greigite diagenesis. *Geophysical Journal International*, 156, 443–458.
- Osterman, L. E. (2003). Benthic foraminifers from the continental shelf and slope of the Gulf of Mexico: An indicator of shelf hypoxia. *Estuarine, Coastal and Shelf Science*, 58, 17–35.
- Pike, C. R., Roberts, A. P., & Verosub, K. L. (1999). Characterizing interactions in fine magnetic particle systems using first order reversal curves. *Journal of Applied Physics*, 85, 6660–6667.
- Qin, Y. S., Zhao, Y. Y., Chen, L. R., & Zhao, S. L. (1987). *Geology of the east China sea* (p. 290). Beijing: China Science Press (in Chinese).
- Rickard, D. (2019). How long does it take a pyrite framboid to form? *Earth and Planetary Science Letters*, 513, 64–68.
- Riedinger, N., Pfeifer, K., Kasten, S., Garming, J. F. L., Vogt, C., & Hensen, C. (2005). Diagenetic alteration of magnetic signals by anaerobic oxidation of methane related to a change in sedimentation rate. *Geochimica et Cosmochimica Acta*, 69, 4117–4126.
- Roberts, A. P. (1995). Magnetic properties of sedimentary greigite (Fe_3S_4). *Earth and Planetary Science Letters*, 134, 227–236.
- Roberts, A. P. (2015). Magnetic mineral diagenesis. *Earth-Science Reviews*, 151, 1–47.
- Roberts, A. P., Almeida, T. P., Church, N. S., Harrison, R. J., Heslop, D., Li, Y. L., et al. (2017). Resolving the origin of pseudo-single domain magnetic behavior. *Journal of Geophysical Research: Solid Earth*, 122, 9534–9558. <https://doi.org/10.1002/2017JB014860>
- Roberts, A. P., Chang, L., Rowan, C. J., Horng, C.-S., & Florindo, F. (2011). Magnetic properties of sedimentary greigite (Fe_3S_4): An update. *Reviews of Geophysics*, 49, RG1002. <https://doi.org/10.1029/2010RG000336>
- Roberts, A. P., Heslop, D., Zhao, X., & Pike, C. R. (2014). Understanding fine magnetic particle systems through use of first-order reversal curve diagrams. *Reviews of Geophysics*, 52. <https://doi.org/10.1002/2014RG000462>

- Roberts, A. P., Liu, Q. S., Rowan, C. J., Chang, L., Carvallo, C., Torrent, J., & Horng, C.-S. (2006). Characterization of hematite (α -Fe₂O₃), goethite (α -FeOOH), greigite (Fe₃S₄), and pyrrhotite (Fe₇S₈) using first-order reversal curve diagrams. *Journal of Geophysical Research: Solid Earth*, 111, B12S35. <https://doi.org/10.1029/2006JB004715>
- Roberts, A. P., & Weaver, R. (2005). Multiple mechanisms of remagnetization involving sedimentary greigite (Fe₃S₄). *Earth and Planetary Science Letters*, 231, 263–277.
- Rochette, P., Fillion, G., Mattéi, J.-L., & Dekkers, M. J. (1990). Magnetic transition at 30–34 Kelvin in pyrrhotite: Insight into a widespread occurrence of this mineral in rocks. *Earth and Planetary Science Letters*, 98, 319–328.
- Rohling, E. J., Foster, G. L., Grant, K. M., Marino, G., Roberts, A. P., Tamisiea, M. E., & Williams, F. (2014). Sea-level and deep-sea-temperature variability over the past 5.3 million years. *Nature*, 508, 477–482.
- Rowan, C. J., & Roberts, A. P. (2006). Magnetite dissolution, diachronous greigite formation, and secondary magnetizations from pyrite oxidation: Unravelling complex magnetizations in Neogene marine sediments from New Zealand. *Earth and Planetary Science Letters*, 241, 119–137.
- Rowan, C. J., Roberts, A. P., & Broadbent, T. (2009). Reductive diagenesis, magnetite dissolution, greigite growth and paleomagnetic smoothing in marine sediments: A new view. *Earth and Planetary Science Letters*, 277, 223–235.
- Saito, Y., Katayama, H., Ikehara, K., Kato, Y., Matsumoto, E., Oguri, K., et al. (1998). Transgressive and highstand systems tracts and post-glacial transgression, the East China Sea. *Sedimentary Geology*, 122, 217–232.
- Shi, X. F., Yao, Z. Q., Liu, Q. S., Larrasoana, J. C., Bai, Y. Z., Liu, Y. G., et al. (2016). Sedimentary architecture of the Bohai Sea China over the last 1 Ma and implications for sea-level changes. *Earth and Planetary Science Letters*, 451, 10–21.
- Skinner, B. J., Erd, R. C., & Grimaldi, F. S. (1964). Greigite, the thio-spinel of iron: A new mineral. *American Mineralogist*, 46, 543–555.
- Usami, K., Ohi, T., Hasegawa, S., & Ikehara, K. (2013). Foraminiferal records of bottom-water oxygenation and surface-water productivity in the southern Japan Sea during 160–15 ka: Associations with insolation changes. *Marine Micropaleontology*, 101, 10–27.
- Verwey, E. J. W. (1939). Electronic conduction of magnetite (Fe₃O₄) and its transition point at low temperature. *Nature*, 144, 327–328.
- Wang, Y. H., Li, G. X., Zhang, W. G., & Dong, P. (2014). Sedimentary environment and formation mechanism of the mud deposit in the central South Yellow Sea during the past 40 kyr. *Marine Geology*, 347, 123–135.
- Wang, Y. H., Zhang, W. G., Liu, X. J., Li, G. X., & Liu, M. (2015). Formation of greigite under different climate conditions in the Yellow River delta. *Science China: Earth Sciences*, 58, 300–308.
- Wu, B., Wu, X. D., Shi, X. F., Qiao, S. Q., Liu, S. F., Hu, L. M., et al. (2020). Influences of tropical monsoon climatology on the delivery and dispersal of organic carbon over the Upper Gulf of Thailand. *Marine Geology*, 426, 106209.
- Xu, T. Y., Shi, X. F., Liu, C. G., Wu, Y. H., Liu, S. F., Fang, X. S., et al. (2020). Stratigraphic framework and evolution of the mid-late Quaternary (since marine isotope stage 8) deposits on the outer shelf of the East China Sea. *Marine Geology*, 419, 106047.
- Xu, T. Y., Shi, X. F., Liu, S. F., Qiao, S. Q., Yao, Z. Q., Fang, X. S., et al. (2018). Late Quaternary sedimentary evolution of the outer shelf of the East China Sea. *Quaternary International*, 493, 59–69.
- Xu, T. Y., Wang, G. Q., Shi, X. F., Wang, X., Yao, Z. Q., Yang, G., et al. (2016). Sequence stratigraphy of the subaqueous Changjiang (Yangtze River) since the Last Glacial Maximum. *Sedimentary Geology*, 331, 132–147.
- Xu, X. D., & Oda, M. (1999). Surface-water evolution of the East China Sea during the last 36,000 years. *Marine Geology*, 156, 285–304.
- Yang, Z. Q., Wang, T. P., Voisin, N., & Copping, A. (2015). Estuarine response to river flow and sea-level rise under future climate change and human development. *Estuarine, Coastal and Shelf Science*, 156, 19–30.
- Yao, Z. Q., Shi, X. F., Liu, Y. G., Kandasamy, S., Qiao, S. Q., Li, X. Y., et al. (2020). Sea-level and climate signatures recorded in orbitally-forced continental margin deposits over the last 1 Myr: New perspective from the Bohai Sea. *Palaeogeography, Palaeoclimatology, Palaeoecology*, 550, 109736.
- Zhang, Q., Liu, Q. S., Li, J. H., & Sun, Y. B. (2018). An integrated study of the eolian dust in pelagic sediments from the North Pacific Ocean based on environmental magnetism, transmission electron microscopy, and diffuse reflectance spectroscopy. *Journal of Geophysical Research: Solid Earth*, 123, 3358–3376. <https://doi.org/10.1002/2017JB014951>
- Zhang, Q., Liu, Q. S., Roberts, A. P., Larrasoana, J. C., Shi, X. F., & Jin, C. S. (2020). Mechanism for enhanced eolian dust flux recorded in North Pacific Ocean sediments since 4.0 Ma: Aridity or humidity at dust source areas in the Asian interior? *Geology*, 48, 77–81.
- Zheng, Y., Kissel, C., Zhang, H. B., Laj, C., & Wang, K. (2010). Sedimentation on the inner shelf of the East China Sea: Magnetic properties, diagenesis and paleoclimate implications. *Marine Geology*, 268, 34–42.